CAD Virtual Human Male Model

Derived from the Visible Human Project of the U.S. National Library of Medicine

for Electromagnetic Safety Evaluations

A Major Qualifying Project Report
Submitted to the Faculty
of the
WORCESTER POLYTECHNIC INSTITUTE
In partial fulfillment of the requirements for the
Degree of Bachelor of Science

By

Patrick Lacroix
&
Nicholas Maino

Submitted to

Dr. Gregory M Noetscher

Dr. Sergey Makarov

April 26, 2017

Abstract

The purpose of this MQP has been to create an accurate cross-platform CAD representation of the male human body for the use in electromagnetic computer simulations. The model is to be employed as a substitute for the human body for SAR (Specific Absorption Rate) estimations. An emerging application includes estimations of the heating rate and temperature rise for embedded metallic implants during a Magnetic Resonance Imaging (MRI) procedure.

During the MQP project period, we have created a manifold CAD model with 233 individual tissue parts in the form of triangular meshes. All tissue parts are true 2-manifold CAD meshes; these meshes do not intersect. The model is being tested in an MRI RF coil using the finite element method based computational electromagnetics software, ANSYS High Frequency Structural Simulator (HFSS).

Acknowledgements

We would like to say thank you to the following people and organizations for their help throughout the project:

- Worcester Polytechnic Institute and the Electrical and Computer Engineering Department for giving us the opportunity to participate in this project.

- Dr. Gregory M Noetscher for mentoring us as well as being available to help whenever we encountered difficulties throughout the project.

- MS Student Harshal Tankaria for his support and guidance throughout the project.

- Dr. Sergey Makarov for both advising the project and being a source of inspiration while completing our project.

Table of Contents

Table of Figures

Table of Tables

Introduction

What Are Virtual Humans

Virtual humans are computer generated three-dimensional models of people. These models are often used to evaluate the effects that real-life applications have on human beings without having to use real life human subjects. This enables researchers to develop equipment and products in a timelier manner and in ways that maximize human safety factors.

There are many different applications where virtual human models can be and are used by researchers to create safe equipment through timely and safe methods. One application that this report focuses on is the use of virtual human models for biomedical simulation applications.

Visible Human Project (VHP)

In 1989, the United States Library of Medicine established the Visible Human Project (VHP). The VHP was tasked with acquiring a complete three-dimensional data set of both the male and female human anatomies. These data sets include both computed tomography (CT) and magnetic resonance images. The data sets of both cadavers were released to the public within one year of each other; the Male model in November 1994, and the Female model in November 1995 [1].

The separation of the male cadaver began by scanning the entire body via Magnetic Resonance Imaging (MRI) and CT. The body was then frozen and cut using 1 millimeter interval. These cuts resulted in over 1,871 slices. Each slice was digitally photographed using a high resolution camera, yielding a total of 15 gigabytes of data. The image shown in Figure 1 is a section view of the VHP Male head. This picture also includes a view of the cerebellum, cerebral

cortex, brainstem, and the nasal passages. The image shown in Figure 2 is a section view of the VHP Male knee, including the patella [2].
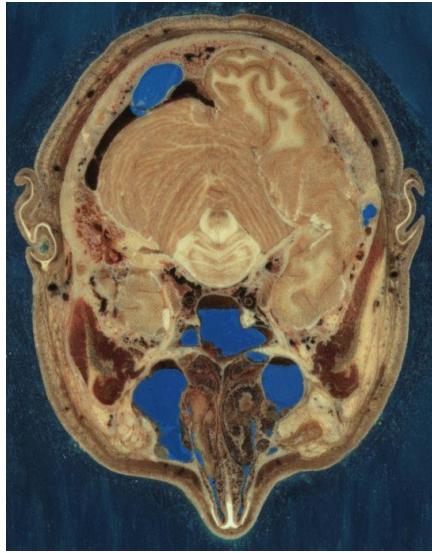
Figure 1: VHP Male Section View of the Head
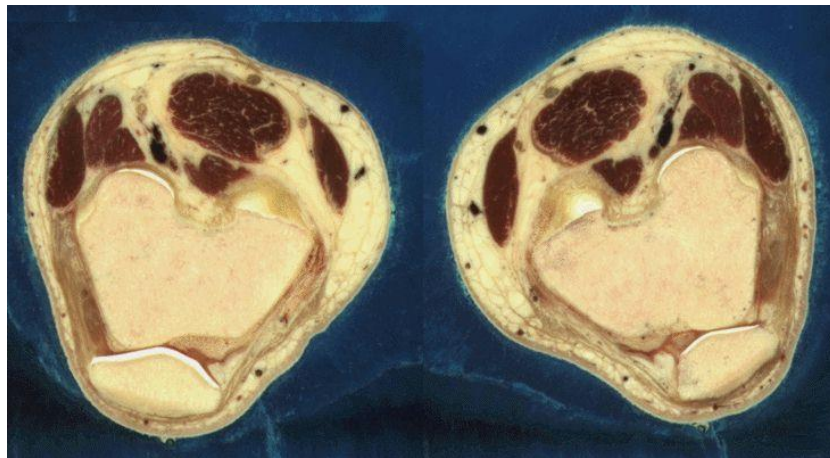
Figure 2: VHP Male Section View of the Knee

The separation of the female cadaver was done almost the same way as the male cadaver. The one difference was cuts in the female cadaver were made using 0.33 millimeter intervals instead of 1 millimeter intervals to match the high resolution digital photography with the CT scan intervals of the female cadaver. This resulted in over 40 gigabytes of photographed data [3].

The male and female data sets are used around the world for many different applications.

Some of these applications include: academic and research purposes, mathematical analysis, medical use, and even virtual reality [1].

Computational Modeling

Computational modeling is the studying of complex systems using computer simulation. These computer simulations involve the use of computer science, mathematics, and physics. Each system being studied is characterized by many different variables. Simulations are conducted by adjusting these characteristics and observing what effects the changes have on the results [4].

The proper observation and recording of model simulations help researchers make accurate predictions on the real-life system being studied if it were subject to the same conditions of the simulation. Modeling can expedite research by allowing scientists to conduct thousands of simulated experiments by computer to identify the actual physical experiments that are most likely to help the researcher find the solution to the problem being studied.

One field of study that uses computational modeling and simulation is the medical industry. According to the Food and Drug Administration, the medical industry uses computational modeling and simulation to help design medical equipment. Areas that often use these studies include: fluid dynamics, solid mechanics, electromagnetics and optics, ultrasound propagation, and thermal propagation. Fluid dynamics uses computational modeling to calculate shear stress in ventricular assist devices. Solid mechanics uses computational modeling for determining the maximum stress locations in a hip implant. Electromagnetics and optics use it to check radiofrequency safety in magnetic resonance imaging. Fluorescence uses it for fiber optic spectroscopy devices. Ultrasound propagation uses it to check the absorbed energy distribution for therapeutic ultrasound. Thermal propagation uses it to observe temperature rises with

radiofrequency and laser ablation devices.

Human models are used in the field of electromagnetics to evaluate the performance and safety of medical devices. Some common medical devices include: electrophysiology monitoring devices, magnetic resonance imaging systems, and magnetic resonance conditional passive or active implanted devices such as orthopedic devices, stents, pacemakers, and neurostimulators [5].

Another example of a research field that uses computational human models is automotive crash safety research. Crash simulations used to be performed using models based on crash-dummies. The main reason for this was because crash safety performances are evaluated using crash test dummies. Since crash dummies differ from the human body in both shape and size, real human body models are more accurate and provide more information. It is believed that a better understanding of injury mechanisms is acquired by using human body models for automotive crash-safety research instead of crash dummies [6].

Constructing VHP-Male

AustinMan

The AustinMan is a virtual human male voxel model that is used for various types of computer simulation applications. He is a high resolution, three-dimensional map of the human body. One application for the AustinMan model is radiation simulation. His use in radiation simulations helps researchers gain an understanding of the potential health-related effects of wireless devices [7].

This virtual human model came into being due to the hard work of both researchers and

students at the University of Texas. The model was assembled from a high-resolution scan of the body of a man on death row who donated his body to science [7].

The AustinMan model is made up of over 100 million three-dimensional pixels called voxels. These voxels interact with each other whenever a virtual cell phone call simulation is run on it. These simulations are designed to predict how various parts of the human body absorb electromagnetic power [7].

To accurately estimate the absorbed power, supercomputers must run complex algorithms on the AustinMan model. He represents the human anatomy through one-millimeter cubed blocks. The researchers worked with anatomists to transform high-resolution image slices into computational maps of the body's tissues. The three images depicted in Figure 3 are of the AustinMan model. The image on the left is a semi-transparent view of the upper organs of the model. The middle image is a depiction of the musculoskeletal structure of the model. The image on the right is a view of the electromagnetic power absorbed at different locations due to the nearby antenna as well as the decibel scale [7].
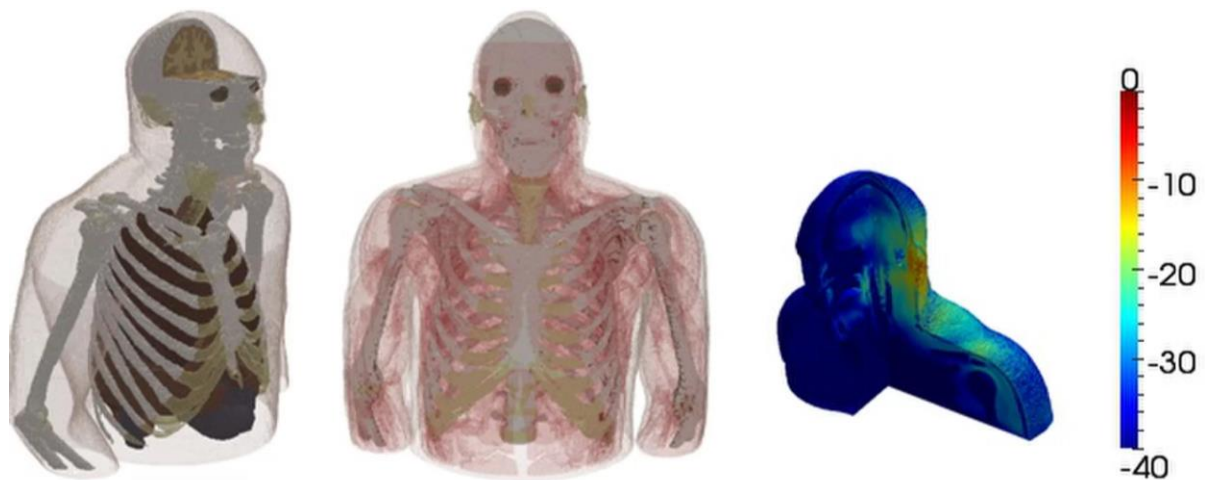
Figure 3: AustinMan Model Upper Organs (left), Musculoskeletal Structure (middle),

Electromagnetic Power Absorption (right)

ISO Surfaces

An ISO surface is a three-dimensional surface that represents points of a constant value within a volume of space. A more mathematical explanation of an ISO surface is: a level set of a continuous function whose domain is three-dimensional space. Some examples of ISO surfaces include: pressure, temperature, velocity, density [8].

ISO surfaces can be used to represent all the volume pixels in an image with a given colocalization level. These points are joined together to form a three-dimensional surface. To better understand ISO surfaces, it is useful to know how they are calculated. When calculating an ISO surface, one must threshold the three-dimensional data set at a certain level. When this is done, the ISO Surface is the resulting surface that surrounds the remaining volume pixels. When this occurs, the volume pixels are distributed into groups. If these groups are not spatially connected, separate surfaces are formed. Every group of connected volume pixels obtained can each be labeled as separate objects. The ISO surface is essentially the surface that surrounds all of those objects [8].

Voxel Models vs. CAD Models

Voxel modeling, or volume pixel modeling, is used to create high quality displays from scalar and vector datasets defined on multidimensional grids. The number of existing voxel human models drastically outnumbers the number of CAD human models with almost 40 total models [9]. Voxel models divide their entire three-dimensional space into unit blocks (cells) of a fixed size. The result of this division is a pixelated tissue volume approximation where each cell has a unique value of tissue properties. A voxel is the designation of the unit cell and its assigned

properties values [8].

Simulations of high resolution voxel models are typically done using Finite Difference Time Domain (FDTD) analysis. In FDTD analysis, electric field vector components in a volume of space are solved at each given instance in time until the desired state of the electromagnetic field is evolved. An alternative method of simulation for virtual models is Finite Element Method (FEM) frequency analysis. FEM subdivides a problem into smaller, simpler problems to yield an approximated result. FEM frequency response simulations solve electric field vector components in a volume of space according to frequency. The reason why FEM frequency analysis is not typically used for higher resolution voxel based models is due to the large memory and processing capability required by computers to run the simulations. The voxel human model's resource intensive FEM frequency domain analysis is the reason why there is a need for an anatomically accurate human model that is capable of efficient FEM frequency domain analysis [8], [9], [10].

Unlike voxel models, CAD models represent ISO surfaces in the form of triangular and quadrilateral meshes, or a boundary representation. This technique is often referred to as three-dimensional surface reconstruction. In a CAD human model, each tissue is characterized by its closed surface. A closed surface is made up of adjacent triangles connected through an array of nodes. All the observation points within a triangulated surface is assigned the same properties unique to the tissue it represents. Since CAD human models are made of triangular meshes, they allow for increasing and decreasing of the resolution of the model. Due to the versatility of CAD human model resolution, researchers can vary the resolution of the model to meet the resource constraints of their computers running the FEM software. The negative effect of decreasing the resolution of the model is that the results of the simulation drop in accuracy. To further

demonstrate the difference between voxel models and CAD models, Figure 4 below shows a side by side comparison of a voxel modeled liver (left) and the same liver modeled in CAD [10], [11].

Figure 4: Liver Voxel Model (Left) and Liver CAD Model (Right)

Mesh Processing

Simply put, a mesh is an interlaced structure. For this application, the term mesh refers to a virtual interlaced structure made up of connected triangles. A result of this project is the generation of virtual meshes that represent all the bones in the human body, specifically the cortical bone, and are suitable for FEM simulations. There are 206 bones in the human adult body. However, only 180 bone meshes were created because certain bones were combined into one bone mesh for simplicity. Generating these bone meshes was a multi-step process of separation, rectification, smoothing, and reduction that started from a rough, unprocessed mesh representing the human male skeleton that was based on the AustinMan model. Figure 5, below, depicts the voxel model skeleton that served as the starting point for this project.

Figure 5: Unprocessed Cortical Bone Skeleton Mesh (Voxel Model)

Watertight and Manifold

The first step in this process was to separate the male skeleton mesh that was provided into individual bone meshes. This involved making copies of bone groups, deleting all but one bone in each group, and exporting that bone mesh. An unfortunate side effect of separating the skeleton into individual bones was that most separated bone meshes contained holes, some small and some large, where they used to connect to other bones. Figure 6, below, depicts the holes that resulted from the separation of the right ulna. Naturally, these holes needed to be filled.
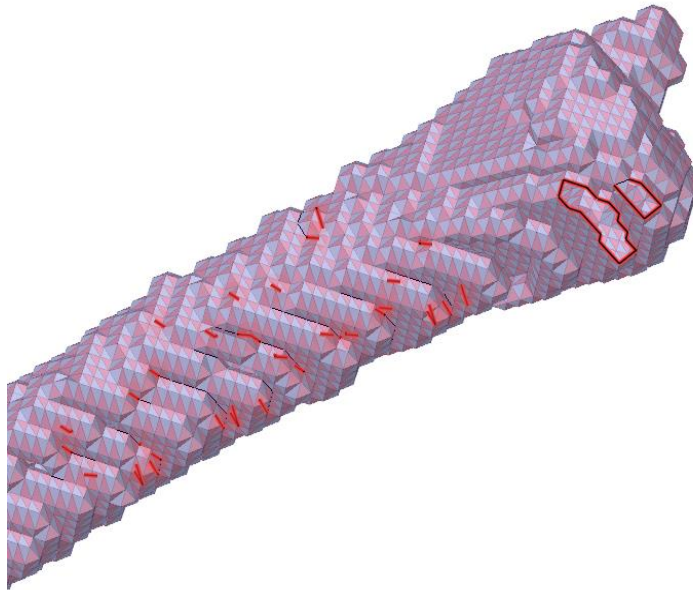
Figure 6: Two holes, highlighted in red, in the right ulna after separation

The original skeleton mesh contained unwanted parts. These parts were either floating pieces that did not belong to any bones or undesirable protrusions of certain bones. Utilizing knowledge of the human bone anatomy, these parts were identified and removed. The protrusions also left holes to be filled in the bone meshes where they were found. Figure 7, below, depicts some of the floating pieces previously mentioned that were part of the original skeleton mesh and were removed. Figure 8, below, depicts a protrusion of the skull that was cut off because it did not belong.

Figure 7: Floating pieces, highlighted in orange, near the sternum
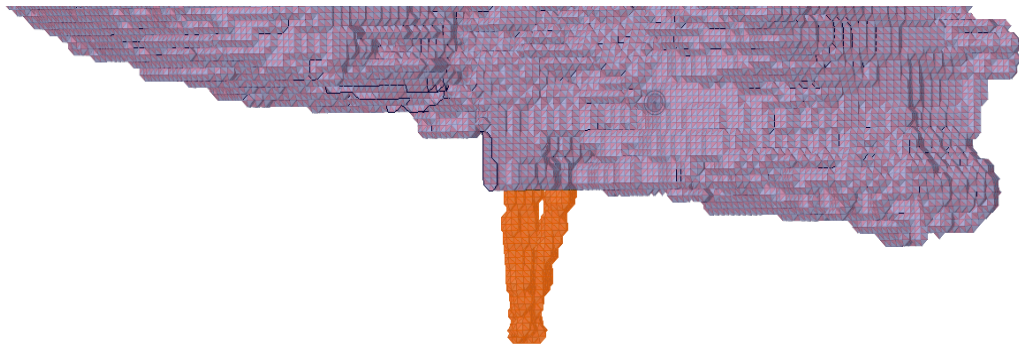
Figure 8: Protrusion, highlighted in orange, located at the bottom of the skull

After separating the skeleton, each bone mesh underwent a thorough cleaning process to prepare it for smoothing. Every bone mesh contained one or all the following issues: not watertight, non-manifold, over-connected, self-intersecting, and multiple pieces. These problems were typically solved in the order previously listed. In more simplified terms, all holes were filled and all unwanted triangles were deleted in each bone mesh.

A mesh is not watertight when it contains holes. To make each bone mesh watertight, every hole in each mesh was filled. Both ANSYS SpaceClaim and Autodesk Meshmixer were used to locate and fill holes in the meshes. Typically, a combination of the "Inspector" tool and "Fill" command in Meshmixer was used due to its ease and versatility with this process. In both programs, filling a hole is as simple as clicking on it after activating the proper tool. Figures 9 and 10, below, depict the use of the Inspector tool in Meshmixer. In Figure 9, the boundaries of the holes are highlighted in red. In Figure 10, the holes have been automatically filled.
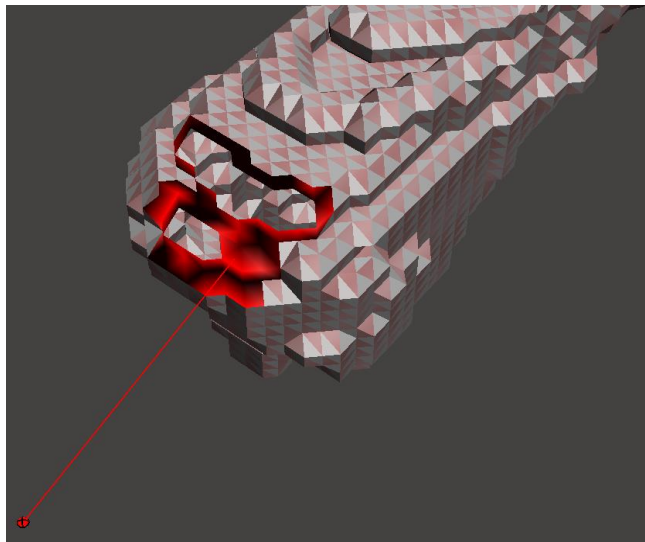
Figure 9: The inspector tool in Meshmixer locating holes in the right ulna mesh
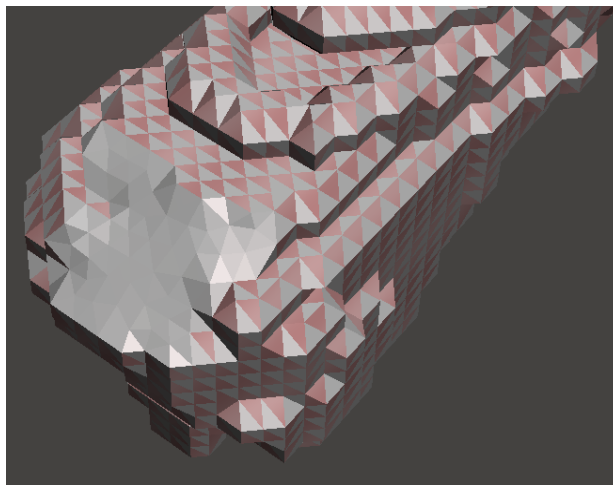
Figure 10: The inspector tool in Meshmixer filling holes in the right ulna mesh

Some large and/or oddly shaped holes had to be fixed in multiple steps to preserve the proper shape of the bone because the one-step automatic fill was unable to produce a desired result. For this, the "Bridge" command in Meshmixer was used to linearly close the gap between two specific triangles. Through this process, smaller holes within a hole were created that could be properly filled with the automatic fill.

Manifold geometry allows disjoint lumps to exist in a single logical body and non-manifold geometry means that all disjoint lumps must be their own logical body [12]. Non-manifold geometry cannot exist in real life which makes it undesirable for a virtual representation of the human body. The separated bone meshes contained non-manifold edges, meaning the meshes were non-manifold. A manifold edge of a triangle is an edge that is connected to only one or two triangle faces. Therefore, a non-manifold edge is connected to more than two triangle faces. A non-manifold vertex is a triangle vertex that is not surrounded by triangle faces. Figure 11, below, depicts an example of a non-manifold edge and an example of non-manifold vertices [43].
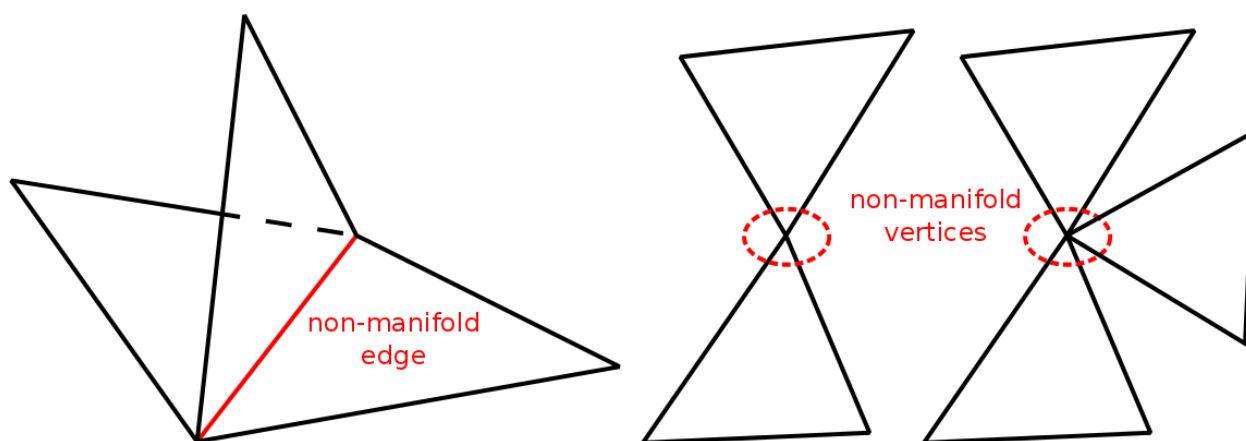
Figure 11: Non-manifold Edge and Vertices Example

Removing non-manifold edges involves deleting the triangles that are causing the problem and filling any holes that result. Non-manifold edges can be located automatically using

CAD software. Instead of removing every non-manifold edge manually, the "Make Solid"

process in Meshmixer was used to automate the process of removing these errors.

Over-connected triangles in a mesh are triangles with at least one side that is connected to

more than one other triangle. Over-connected triangles in a mesh are automatically detected by

Meshmixer and their edges are automatically highlighted. Using Meshmixer, over-connected

triangles were identified and removed from each bone mesh when necessary. Figure 12, below,

depicts the automatic detection of over-connected triangles in Meshmixer.
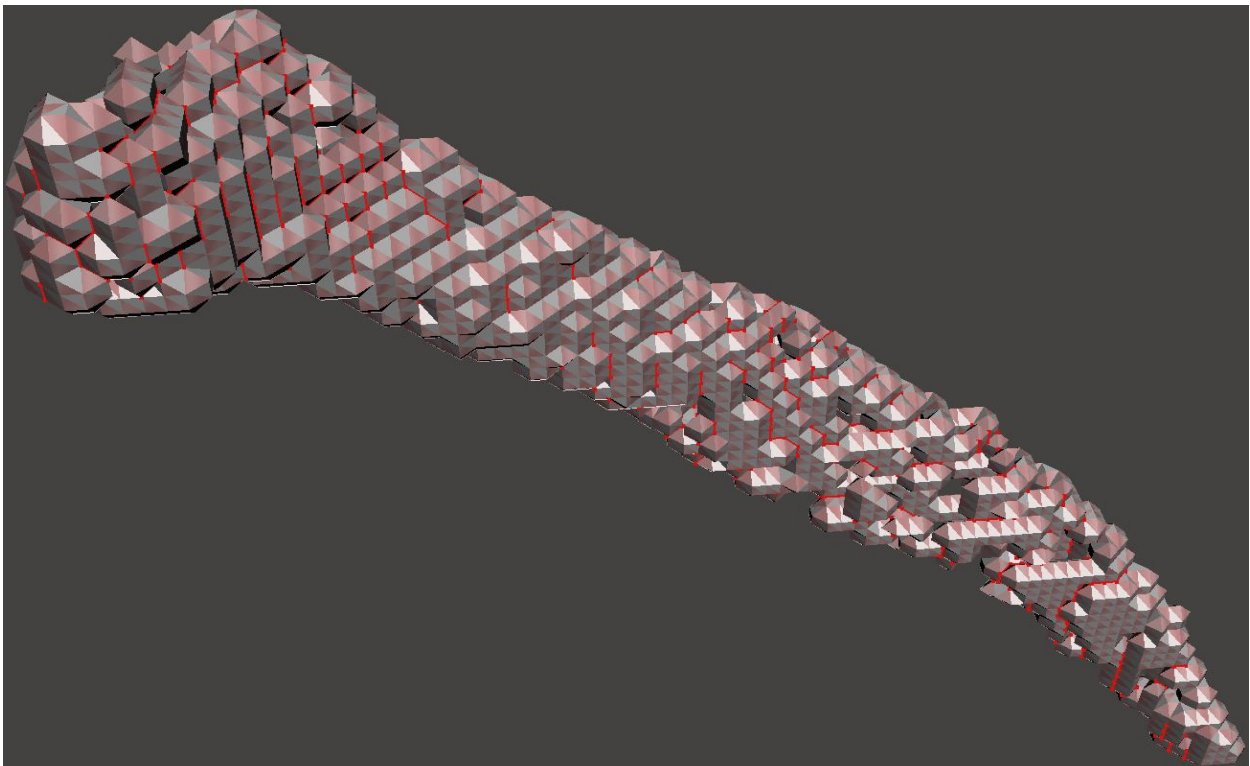
Figure 12: Over-connected triangle edges, highlighted in red, being detected in Meshmixer

Self-intersecting triangles in a mesh are triangles that overlap with each other; in other

words, they try to occupy the same space. The "Intersections" tool in SpaceClaim was used to

locate self-intersecting triangles, which were then fixed by deleting the extra triangles. Figure 13,

below, depicts the use of the "Intersections" tool in SpaceClaim to identify self-intersecting
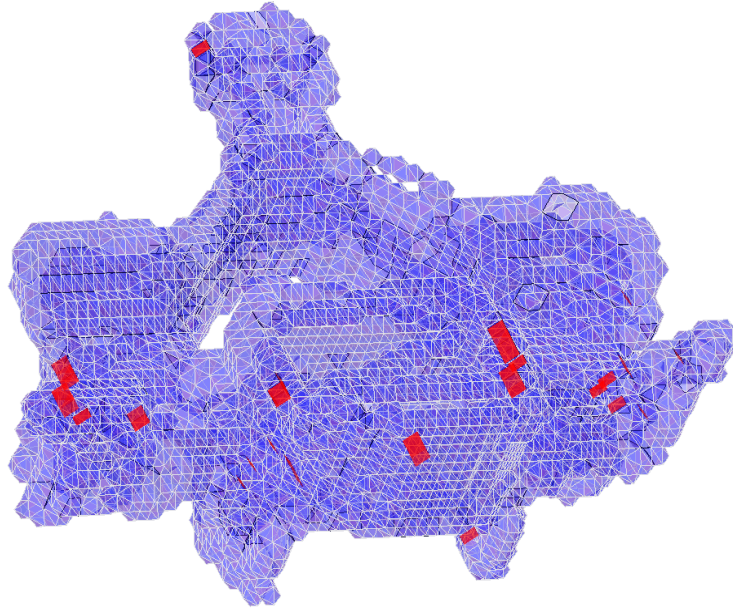
triangles.

Figure 13: Self-intersecting triangles, highlighted in red, being detected in SpaceClaim

The "Separate All" command in SpaceClaim was used to separate individual bodies within a mesh. This tool was used to locate the unwanted, floating pieces mentioned previously during the separation process. It was also used to identify unwanted bodies located inside the walls of the bone in some bone meshes so that they could be deleted to fix the error of having multiple pieces in one mesh.

In some bone meshes, inner shells were formed that would connect to the outer shell of the bone in one or more places. These places of connection were identified and triangles were deleted so that these two shells were no longer connected. After separating the shells, the resulting holes were patched up and the mesh was separated into its individual bodies. From this point, the unwanted inner shell could be deleted entirely. Having every bone mesh contain only the outer shell is desirable for simulation accuracy and runtime. Figure 14, below, depicts an example of a separate body that was deleted from the skull mesh. This inner shell had to be manually disconnected from the outer shell before it could be separated and deleted entirely.
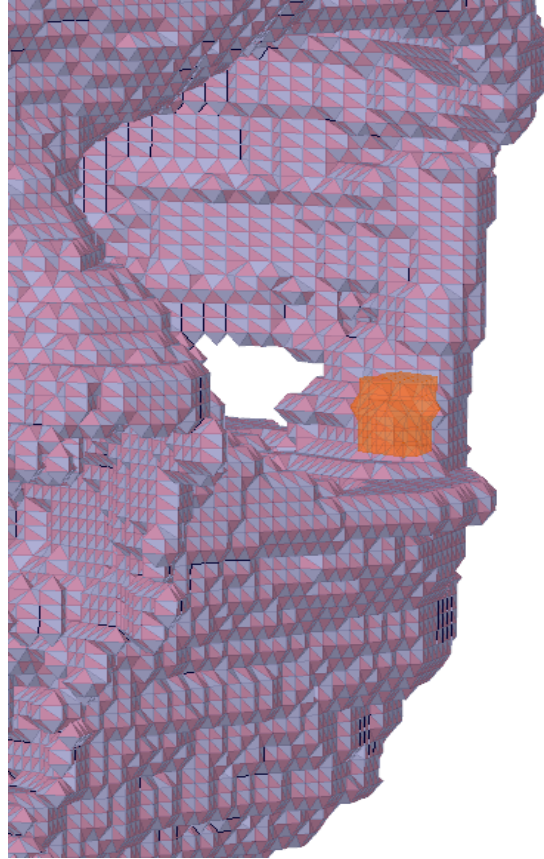
Figure 14: Separate body (inner shell), highlighted in orange, in the skull

Surface Reconstruction

After getting the bone meshes to meet the conditions of being watertight and manifold,

the process of surface reconstruction began. Prior to surface reconstruction, the meshes were

jagged and blocky. Surface reconstruction dramatically reduces the roughness of the surface of

the mesh and shapes it more like the actual bone it represents. Doing so increases the accuracy of

simulation results but also increases the number of triangles that make up the mesh. Smoother

surfaces require the generation of more triangles and more triangles require longer simulation

runtimes. Therefore, it is necessary to find a balance between the smoothness of the surface of a

mesh and the number of triangles required to generate that smooth surface. Thus, surface

smoothing and triangle decimation are both required to reconstruct the surfaces of the processed

bone meshes.

"Poisson Surface Reconstruction" in MeshLab was used to smooth the surfaces of the bone meshes. This smoothing process contains multiple parameters that can be adjusted for different results. A lot of trial and error went into discovering the ideal parameters for each mesh. Losing a small amount of volume from each bone was an unfortunate side effect of using Poisson Surface Reconstruction on the meshes. Figure 15, below, depicts the smoothed mesh of the skull that resulted from the application of Poisson Surface Reconstruction in MeshLab.
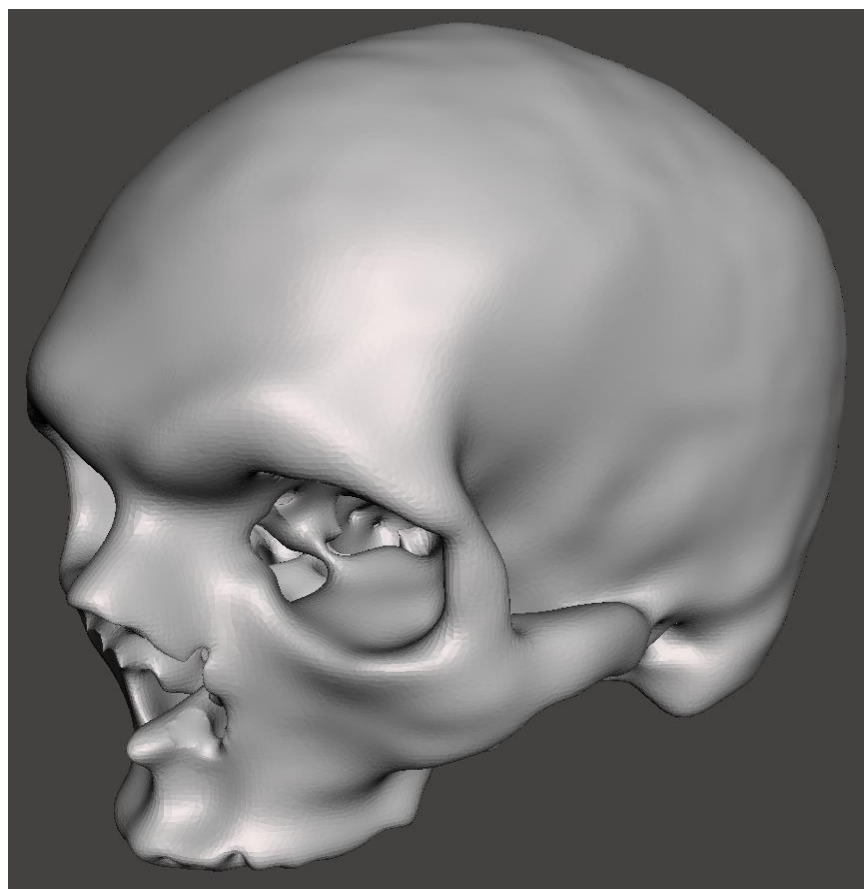
Figure 15: Smoothed Skull Mesh

MeshLab was also used to decimate the surfaces of the bone meshes after the smoothing was done. The smooth surfaces were decimated to the point just before the surface of the mesh starts to misrepresent the surface of the bone it characterizes. In other words, the number of

triangles in each mesh was reduced enough to maintain the proper shape of the bone as well as realistic simulation runtimes. Figure 16, below, depicts the decimated version of the skull mesh. Ideally, for the most accurate results, the bone mesh surfaces would be smoothed to perfection with no triangle decimation. This was not done because running simulations on such meshes would require an unrealistic amount of both time and computer hardware.

Figure 16: Decimated Skull Mesh

Available Tools

Among the tools available to us for this project we chose to use ANSYS SpaceClaim, Autodesk Meshmixer, and MeshLab. In Atwater Kent Laboratories at WPI, we were granted access to a desktop computer with SpaceClaim installed. With this we accessed a single shared license of SpaceClaim. Meshmixer and MeshLab are both free software that we could use with

any computer at any time. SpaceClaim and Meshmixer were used for their rectification tools that allowed us to make meshes manifold and watertight. MeshLab was used for its smoothing and decimation algorithms to perform surface reconstruction on meshes. This combination of 3D modeling software tools proved effective and time-efficient for the mesh processing required for this project.

Resulting Model

To create the final model for this project, the VHP-Male FEM CAD Model, the cortical bone meshes that were created were combined with other meshes that were previously created by other students that represent the VHP-Male skin, cartilage, and organs. Not all cartilage layers and organs are included in this model. Figure 17, below, depicts an image of the model where only the skin layer is visible. Figures 18, 19, and 20 depict the model at various viewpoints where the skin layer is transparent, the cortical bone is white, the cartilage is grey, and the included organs are pink. Finally, Table 1 is a list of every individual mesh included in the model, color coded by tissue type and sorted alphabetically, with the corresponding number of triangles, mesh quality, and minimum edge length for each mesh.

Figure 17: VHP-Male FEM CAD Model Skin Only View
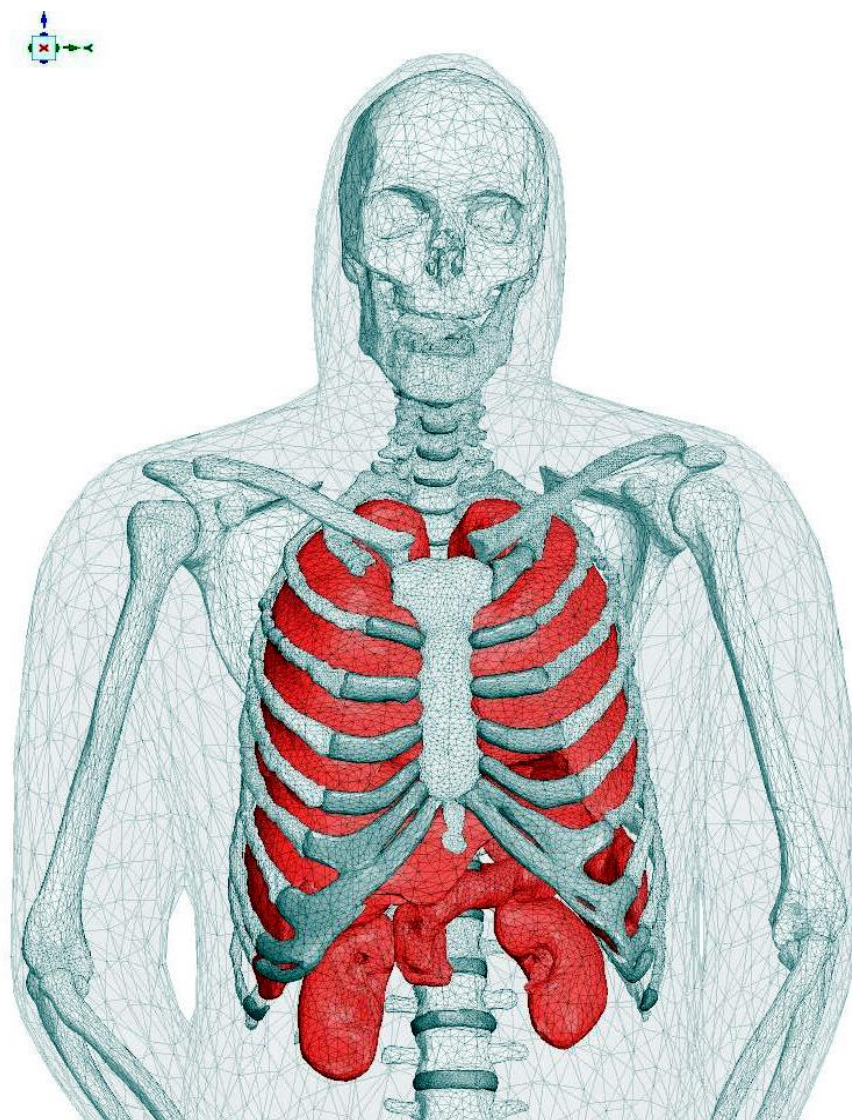
Figure 18: VHP-Male FEM CAD Model Skeleton Chest View
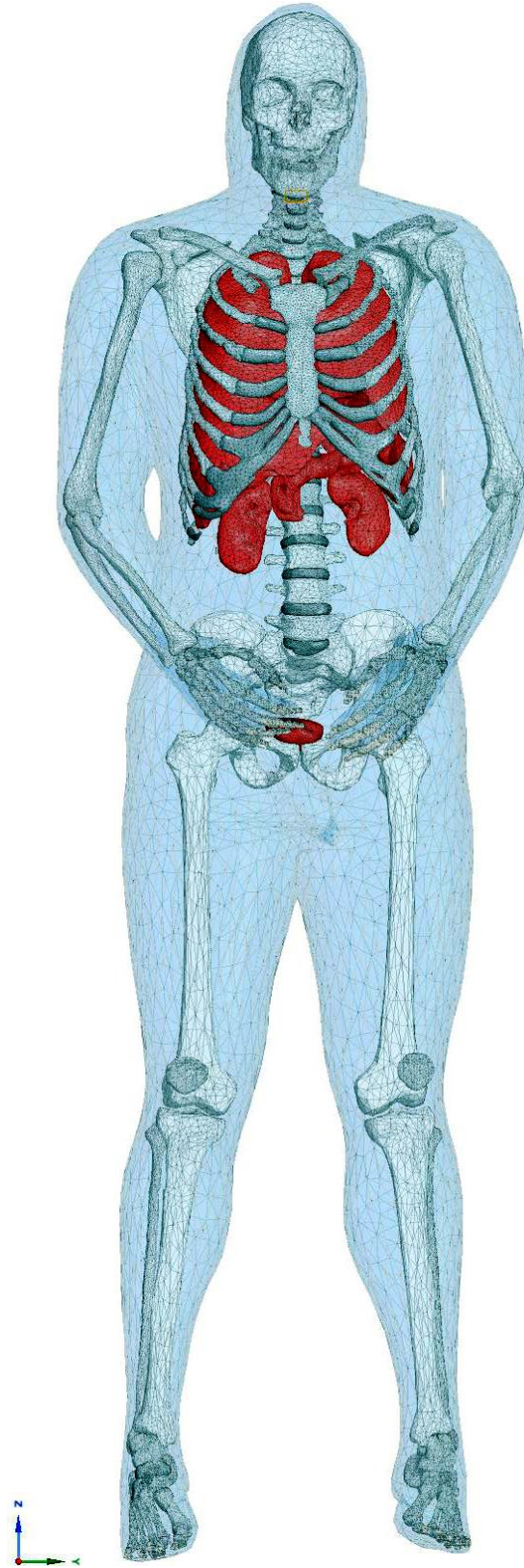
Figure 19: VHP-Male FEM CAD Model Front View
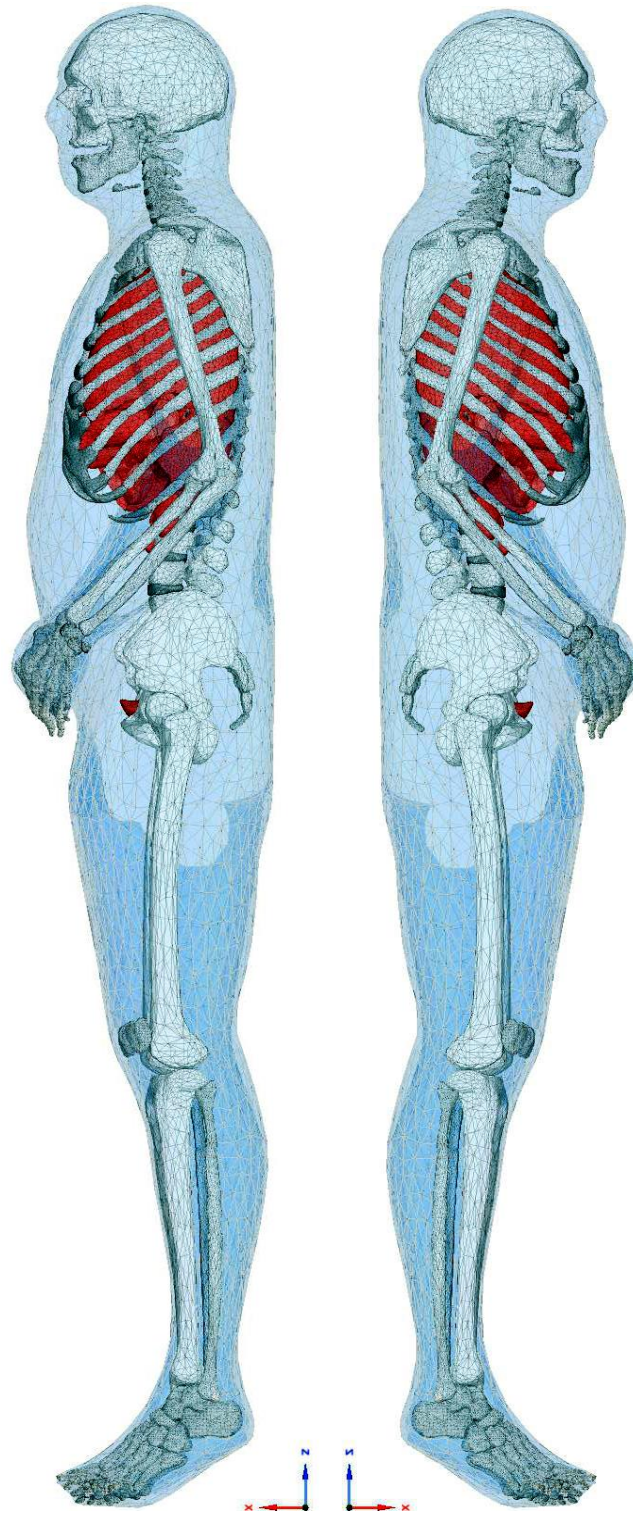
Figure 20: VHP-Male FEM CAD Model Left (Left) & Right (Right) View

Table 1: List of Triangular Surface Meshes – Version 1.0

VHP-Male FEM CAD Model version 1.0 April. 2017

Legend:

Hard tissues	Soft tissues	Individual muscles	Cartilage	Titanium	Nervous tissues

Mesh no	Tissue name	Triangle size	Mesh quality	Min. Edge Length
1	AM Bladder	1748	0.165843512	1.146289401
2	AM Brain White Matter	6822	0.00410152	1.104397332
3	AM Calcaneus Left	6342	0.01849233	0.166343998
4	AM Calcaneus Right	6594	0.00883073	0.096854562
5	AM Capitate Left	1290	0.115956658	0.609177938
6	AM Capitate Right	1236	0.178687667	0.743911627
7	AM Cerebellum	6320	0.058905114	0.673282885
8	AM Clavicle Left	5872	0.005939045	0.105782511
9	AM Clavicle Right	1618	0.056005161	1.18798056
10	AM Coccyx	1388	0.023502358	0.246121452
11	AM Cuboid Left	2046	0.120454862	0.234047264
12	AM Cuboid Right	2514	0.008202353	0.335261223
13	AM Cuneiform Intermediate Left	1846	0.003170746	0.189465083
14	AM Cuneiform Intermediate Right	2920	0.000965018	0.000745185
15	AM Cuneiform Lateral Left	1264	0.001772575	0.002655347
16	AM Cuneiform Lateral Right	1772	0.075727161	0.540076619
17	AM Cuneiform Medial Left	1510	0.048780475	0.24856055
18	AM Cuneiform Medial Right	1456	0.014741385	0.407812655
19	AM DiscC03C04	856	0.305478073	0.584580433
20	AM DiscC04C05	700	0.294796604	0.710019675
21	AM DiscC05C06	738	0.316159564	0.756420333

Mesh no	Tissue name	Triangle size	Mesh quality	Min. Edge Length
22	AM DiscC06C07	718	0.180940582	0.768648629
23	AM DiscC07T01	622	0.1184832	0.560222652
24	AM DiscL01L02	2814	0.169732925	0.545922493
25	AM DiscL02L03	3062	0.166660311	0.582298467
26	AM DiscL03L04	3070	0.130098278	0.679224789
27	AM DiscL04L05	2888	0.100150214	0.65616874
28	AM DiscL05L06	2650	0.105528846	0.689811312
29	AM DiscL06S00	2786	0.268538785	0.702797035
30	AM DiscS01	624	0.210085898	19.43617431
31	AM DiscS02	260	0.570149846	16.39392215
32	AM DiscS03	218	0.59287632	0.579131673
33	AM DiscS04	190	0.604148056	18.47601168
34	AM DiscT01T02	628	0.237890065	0.776213193
35	AM DiscT02T03	606	0.28529372	0.926420859
36	AM DiscT03T04	688	0.164562872	0.835285812
37	AM DiscT04T05	766	0.357124765	0.721534423
38	AM DiscT05T06	758	0.16421495	0.776179996
39	AM DiscT06T07	730	0.306740968	0.856165141
40	AM DiscT07T08	754	0.239607771	0.768537297
41	AM DiscT08T09	770	0.173574419	0.928438558
42	AM DiscT09T10	848	0.189534648	0.972885705
43	AM DiscT10T11	744	0.251148608	1.013260169
44	AM DiscT11T12	824	0.288589886	1.140370543
45	AM DiscT12L01	2792	0.077715317	0.409742153
46	AM Femur Left	1094	0.00534762	3.266816029
47	AM Femur Right	1294	0.018471356	2.724684681
48	AM Fibula Left	4062	0.000323293	0.617614174
49	AM Fibula Right	4600	0.018591138	0.645111333

Mesh no	Tissue name	Triangle size	Mesh quality	Min. Edge Length
50	AM Gall Bladder	980	0.107164257	1.538768738
51	AM Hamate Left	1042	0.143223341	0.722980504
52	AM Hamate Right	1284	0.005305109	0.65315022
53	AM Hip Left	1186	0.008574512	2.479635443
54	AM Hip Right	1718	0.003301394	2.28230427
55	AM Humerus Left	1710	0.00451329	1.543380871
56	AM Humerus Right	3678	0.010896982	0.35741476
57	AM Hyoid	2106	0.001241288	0.185893971
58	AM Kidney Left	1738	0.103633477	0.475712171
59	AM Kidney Right	1510	0.180670718	0.568609335
60	AM Liver	4674	3.32858E-05	0.000375317
61	AM Lunate Left	968	0.016093839	0.014566606
62	AM Lunate Right	992	0.000315972	0.000307077
63	AM Lung Left	7564	1.98621E-05	3.41197E-05
64	AM Lung Right	7150	0.07105748	1.166709667
65	AM Mandible	12076	0.000633624	0.437681409
66	AM Metacarpal Left1	1980	0.024224086	0.177440957
67	AM Metacarpal Left2	2234	0.143783503	0.694911928
68	AM Metacarpal Left3	2350	0.060616727	0.2559417
69	AM Metacarpal Left4	1560	0.103910186	0.654534744
70	AM Metacarpal Left5	2116	0.005326187	0.005008696
71	AM Metacarpal Right1	2502	0.096276603	0.094777462
72	AM Metacarpal Right2	2008	0.094986164	0.623438972
73	AM Metacarpal Right3	2038	0.130443935	0.794260829
74	AM Metacarpal Right4	1838	0.073447379	0.202081024
75	AM Metacarpal Right5	1550	0.027619579	0.185875474
76	AM Metatarsal Left1	2156	0.013289397	0.878610082
77	AM Metatarsal Left2	1626	0.099438677	0.811484518

Mesh no	Tissue name	Triangle size	Mesh quality	Min. Edge Length
78	AM Metatarsal Left3	1454	0.057045165	0.546636831
79	AM Metatarsal Left4	1800	0.014347948	0.544737943
80	AM Metatarsal Left5	1544	0.12018651	0.852837499
81	AM Metatarsal Right1	1974	0.060598035	0.56842732
82	AM Metatarsal Right2	1558	0.110406538	0.836171019
83	AM Metatarsal Right3	1690	0.092595703	0.401816542
84	AM Metatarsal Right4	1664	0.117268689	0.749947902
85	AM Metatarsal Right5	2154	0.071209879	0.587167763
86	AM Navicular Left	1360	0.08137763	0.658380289
87	AM Navicular Right	2786	0.120202896	0.44683947
88	AM Pancreas	2444	0.045940441	0.745068684
89	AM Patella Left	2390	0.009060994	0.280281871
90	AM Patella Right	2502	0.046052626	0.736421856
91	AM Phalange Distal Foot Left1	1576	0.108010025	0.173872181
92	AM Phalange Distal Foot Left2	1056	0.013961018	0.00806157
93	AM Phalange Distal Foot Left3	936	0.008312845	0.004756534
94	AM Phalange Distal Foot Left4	304	0.008453153	0.00763092
95	AM Phalange Distal Foot Left5	304	0.001680509	0.001753542
96	AM Phalange Distal Foot Right1	1462	0.165436026	0.284162432
97	AM Phalange Distal Foot Right2	1212	0.00236099	0.00106316
98	AM Phalange Distal Foot Right3	1064	0.011167542	0.005352356
99	AM Phalange Distal Foot Right4	276	0.050130111	0.044166955
100	AM Phalange Distal Foot Right5	268	0.00921589	0.010257327
101	AM Phalange Distal Hand Left1	1020	0.006748611	0.006526554
102	AM Phalange Distal Hand Left2	608	0.025708565	0.023325673
103	AM Phalange Distal Hand Left3	642	0.001380528	0.002028903
104	AM Phalange Distal Hand Left4	476	0.006707068	0.005847044
105	AM Phalange Distal Hand Left5	584	0.023649217	0.014946917

Mesh no	Tissue name	Triangle size	Mesh quality	Min. Edge Length
106	AM Phalange Distal Hand Right1	1412	0.11692216	0.245557164
107	AM Phalange Distal Hand Right2	608	0.017402547	0.013066549
108	AM Phalange Distal Hand Right3	692	0.00281707	0.002100177
109	AM Phalange Distal Hand Right4	714	0.004499034	0.004302437
110	AM Phalange Distal Hand Right5	636	0.004514525	0.003352631
111	AM Phalange Intermediate Foot Left2	820	0.010826263	0.006794707
112	AM Phalange Intermediate Foot Left3	690	0.218476507	0.153918786
113	AM Phalange Intermediate Foot Left4	880	0.001434312	0.001375409
114	AM Phalange Intermediate Foot Left5	1316	0.002289162	0.00141373
115	AM Phalange Intermediate Foot Right2	822	0.385629735	0.517597619
116	AM Phalange Intermediate Foot Right3	992	0.003053593	0.001919577
117	AM Phalange Intermediate Foot Right4	1132	0.002877368	0.001351157
118	AM Phalange Intermediate Foot Right5	296	0.018398879	0.023237014
119	AM Phalange Intermediate Hand Left2	1162	0.181987259	0.178802675
120	AM Phalange Intermediate Hand Left3	1040	0.09454119	0.293702795
121	AM Phalange Intermediate Hand Left4	1030	0.106718986	0.391615608
122	AM Phalange Intermediate Hand Left5	770	0.007202779	0.017305512
123	AM Phalange Intermediate Hand Right2	1250	0.079557617	0.231832526
124	AM Phalange Intermediate Hand Right3	1048	0.133530746	0.394320825
125	AM Phalange Intermediate Hand Right4	1102	0.004467088	0.091368069
126	AM Phalange Intermediate Hand Right5	1010	0.025343714	0.251865618
127	AM Phalange Proximal Foot Left1	1180	0.067250547	0.155431202
128	AM Phalange Proximal Foot Left2	1430	0.041488749	0.12106594
129	AM Phalange Proximal Foot Left3	1640	0.375804216	0.557077013
130	AM Phalange Proximal Foot Left4	1604	0.40733488	0.37944973
131	AM Phalange Proximal Foot Left5	1410	0.039294339	0.030789055

Mesh no	Tissue name	Triangle size	Mesh quality	Min. Edge Length
132	AM Phalange Proximal Foot Right1	1288	0.056069761	0.37548778
133	AM Phalange Proximal Foot Right2	1090	0.18447097	0.352734587
134	AM Phalange Proximal Foot Right3	1148	0.0130454	0.229914032
135	AM Phalange Proximal Foot Right4	1244	0.075053789	0.309842275
136	AM Phalange Proximal Foot Right5	1532	0.399308487	0.394715192
137	AM Phalange Proximal Hand Left1	1416	0.199237756	0.282433564
138	AM Phalange Proximal Hand Left2	1016	0.022168995	0.266357983
139	AM Phalange Proximal Hand Left3	1338	0.070157467	0.285585063
140	AM Phalange Proximal Hand Left4	1204	0.127832394	0.145829967
141	AM Phalange Proximal Hand Left5	2072	0.004604116	0.003282591
142	AM Phalange Proximal Hand Right1	1148	0.056622782	0.294785727
143	AM Phalange Proximal Hand Right2	1352	0.015077543	0.209916702
144	AM Phalange Proximal Hand Right3	1616	0.051939832	0.719380595
145	AM Phalange Proximal Hand Right4	1138	0.043604735	0.1649986
146	AM Phalange Proximal Hand Right5	1174	0.013977571	0.188347219
147	AM Pisiform Left	1184	0.500552373	0.515689782
148	AM Pisiform Right	1128	0.401400298	0.611734152
149	AM Radius Left	1560	0.002802002	0.934970278
150	AM Radius Right	1754	0.010033257	1.214635887
151	AM Rib1Left	5000	0.071257887	0.303154488
152	AM Rib1Right	2774	0.008231877	0.025456508
153	AM Rib2Left	5000	0.012364259	0.24600827
154	AM Rib2Right	2470	0.019798289	0.478469991
155	AM Rib3Left	5028	0.009869838	0.055562581
156	AM Rib3Right	5120	0.011922806	0.093057078
157	AM Rib4Left	2506	0.021756632	0.884217361
158	AM Rib4Right	2504	0.039284326	1.031816028
159	AM Rib5Left	5000	0.000922563	0.063404806

Mesh no	Tissue name	Triangle size	Mesh quality	Min. Edge Length
160	AM Rib5Right	2380	0.00162164	0.777948568
161	AM Rib6Left	5008	0.03157469	0.243544913
162	AM Rib6Right	5026	0.030315918	0.334360249
163	AM Rib7Left	2510	0.03593509	0.61452184
164	AM Rib7Right	2290	0.02321827	0.436906477
165	AM Rib8Left	2496	0.034966755	0.620124523
166	AM Rib8Right	2470	0.035852455	0.814331668
167	AM Rib9Left	5026	0.033871361	0.259944831
168	AM Rib9Right	2488	0.007762291	0.869718583
169	AM Rib10Left	5018	0.001194147	0.201178192
170	AM Rib10Right	2518	0.026009228	0.382919008
171	AM Rib11Left	2384	0.017592626	0.633465069
172	AM Rib11Right	2402	0.037767592	0.614755961
173	AM Rib12Left	2022	0.067914088	0.232126753
174	AM Rib12Right	2824	0.0003394	0.000845212
175	AM RibLeft01 Cartilage	892	0.195572578	0.239014677
176	AM RibLeft02 Cartilage	254	0.153906719	1.842955792
177	AM RibLeft03 Cartilage	724	0.195516456	1.000557231
178	AM RibLeft04 Cartilage	650	0.188959263	1.134851109
179	AM RibLeft05 Cartilage	650	0.165867027	1.497202678
180	AM RibLeft06 09 Cartilage	1792	0.100098473	0.591946184
181	AM RibLeft10 Cartilage	466	0.383969375	0.657494161
182	AM RibRight02 Cartilage	600	0.231056419	0.808358036
183	AM RibRight03 Cartilage	600	0.166468653	1.143019274
184	AM RibRight04 Cartilage	600	0.250344623	1.179451485
185	AM RibRight05 Cartilage	600	0.307728065	1.367763382
186	AM RibRight06 09 Cartilage	1900	0.102953268	1.104599593
187	AM RibRight10 Cartilage	410	0.187648969	0.881692954

Mesh no	Tissue name	Triangle size	Mesh quality	Min. Edge Length
188	AM Sacrum	7146	0.005022698	0.121273699
189	AM Scaphoid Left	2906	0.042625118	0.389046161
190	AM Scaphoid Right	2808	0.229988786	0.325345446
191	AM Scapula Left	2118	0.002681555	0.905832545
192	AM Scapula Right	2064	0.003680874	0.996482213
193	AM Skin	8842	0.022628312	3.970350748
194	AM Skull	14766	0.001814466	0.154270982
195	AM SpineC1	2940	0.009889099	0.775889177
196	AM SpineC2	1538	0.067767241	1.02994847
197	AM SpineC3	2046	0.028864561	0.61426171
198	AM SpineC4	4906	0.01442564	0.365475714
199	AM SpineC5	6034	0.000406313	0.442266939
200	AM SpineC6	5166	0.019284117	0.534809148
201	AM SpineC7	1894	0.037704211	0.694765605
202	AM SpineL1	4420	1.97067E-05	0.001748863
203	AM SpineL2	2054	0.006781578	1.047850941
204	AM SpineL3	1432	0.01101174	1.340544755
205	AM SpineL4	3652	0.003935922	0.372751269
206	AM SpineL5	1838	0.002179277	1.503357261
207	AM SpineT1	1714	0.007187073	0.612626323
208	AM SpineT2	2462	0.004042741	0.230125351
209	AM SpineT3	2302	0.047430177	0.087896055
210	AM SpineT4	1770	0.011246387	0.824654356
211	AM SpineT5	1846	0.076254931	0.738770781
212	AM SpineT6	1274	0.133359981	0.902911234
213	AM SpineT7	1186	0.077370099	1.343114682
214	AM SpineT8	4240	0.033883063	0.611967842
215	AM SpineT9	2226	0.004931268	0.7826207

Mesh no	Tissue name	Triangle size	Mesh quality	Min. Edge Length
216	AM SpineT10	1718	0.006038069	0.928004894
217	AM SpineT11	1954	0.027706186	0.769982968
218	AM SpineT12	2642	0.029793464	0.997643381
219	AM Spleen	3808	0.056448557	1.286415849
220	AM Sternum	4610	0.07959315	0.732095776
221	AM Talus Left	3398	0.000559035	0.597655072
222	AM Talus Right	3388	0.081121069	0.65055969
223	AM Thymus	2980	0.20530693	0.513102396
224	AM Tibia Left	1366	0.001575822	2.060671952
225	AM Tibia Right	1686	0.001500973	1.747887591
226	AM Trapezium Left	1964	0.066308959	0.263223813
227	AM Trapezium Right	3200	0.008485069	0.004995687
228	AM Trapezoid Left	906	0.00093608	0.000805687
229	AM Trapezoid Right	760	0.040665661	0.039996476
230	AM Triquetral Left	2218	0.000318628	0.035252136
231	AM Triquetral Right	1182	0.000738741	0.000580035
232	AM Ulna Left	2180	0.010992618	1.012463565
233	AM Ulna Right	2342	0.032245387	1.002866313

EM Simulations using the VHP-Male Computational Phantom

Computational phantoms provide insight into the response of the human body to a variety of external stimuli that would not be possible using non-invasive experimental methods. Examples include evaluating current densities along the surface of the brain experienced during non-invasive brain stimulation via Transcranial Magnetic Stimulation [19][20], assessing local heating due to RF exposure [21]-[23] and estimating the Specific Absorption Rate (SAR) within a patient undergoing a Magnetic Resonance Imaging (MRI) procedure [24]-[42]. We have

applied the new VHP-Male model to this last application to demonstrate one of the many

potential uses a CAD-based model can have to the academic and medical communities.

MRI Coil Design

The MRI coil used in the simulation is given below in Figure 21. It is a high-pass bird

cage design consisting of 16 rungs and all dimensions are provided in Table 2 below; these have

been parameterized to enable optimization of the coil design in future simulations. All metallic

structures were modeled with the electrical properties of copper (relative permittivity of 1,

conductivity of 5.8e7 siemens/meter). The coil was fed through 32 ports (16 on top and 16 on the

bottom) through a novel method to establish a highly uniform magnetic field at the coil center.
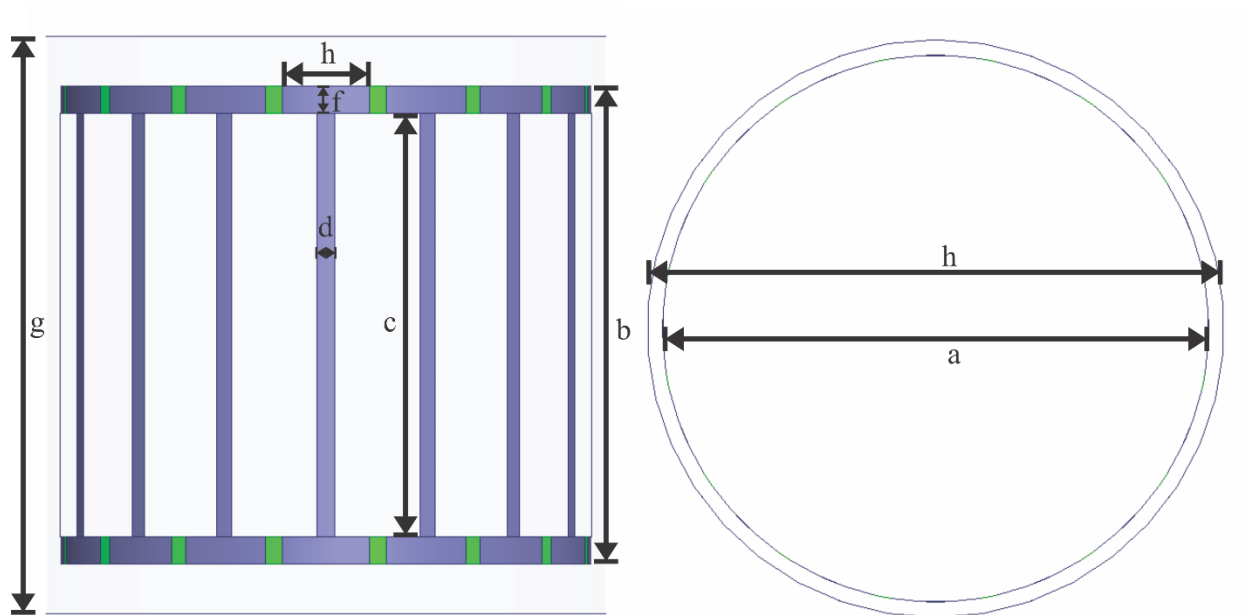
Figure 21: A generic 16-rung high-pass coil [24] to be used as a substitute for multichannel

coils (Coil dimensions are shown in Table 2)

Table 2: Parameterized coil dimensions of the generic high-pass coil [24] (All lengths given in mm)

Number of Rungs	a = Coil Diameter	b = Coil Height	c = Rung length	d = Rung Width	e = Endring segment	f = Endring Width	g = Shield Height	h = Shield Inner Diam	i = Shield Outer Diam	Operating Freq (MHz)
16	740	650	610	25	135	40	847	705	824	64

Simulation Settings

All simulations were conducted using ANSYS Electronics Desktop 2016.2.0 on a high-performance work station running Windows Server 2008 R2 Enterprise. The work station consisted of 64 AMD Opteron Processor 6380 CPUs running at 2.50 GHz and a total of 512 GB of RAM.

The model driven solution was found at 64 MHz using 8 passes of adaptive mesh refinement. In this way, more tetrahedral elements were added to the simulation space to produce solution convergence. A maximum refinement percentage of 30% pass to pass was specified. An example of mesh refinement values and the resulting convergence is given below in Table 3.

Figure 22, below, shows various views of the coil loaded with the VHP-Male computational phantom. All simulations were conducted at the abdomen landmark and the ends of the MRI shield were covered in a Perfect Matched Layer (PML) to minimize wave reflections in the simulation domain, shown below in Figure 23, which also depicts the surrounding MRI shield, again modeled as copper material.
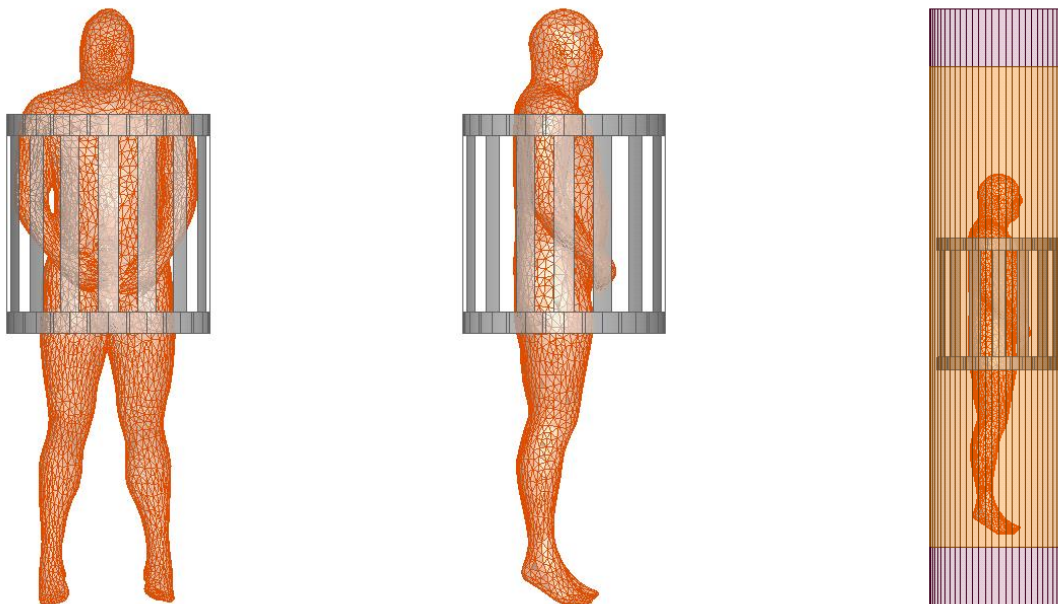
Figure 22: The MRI coil loaded with the VHP-Male computational phantom: front (left), right

(center), and with surrounding MRI shield and boundary conditions (right)
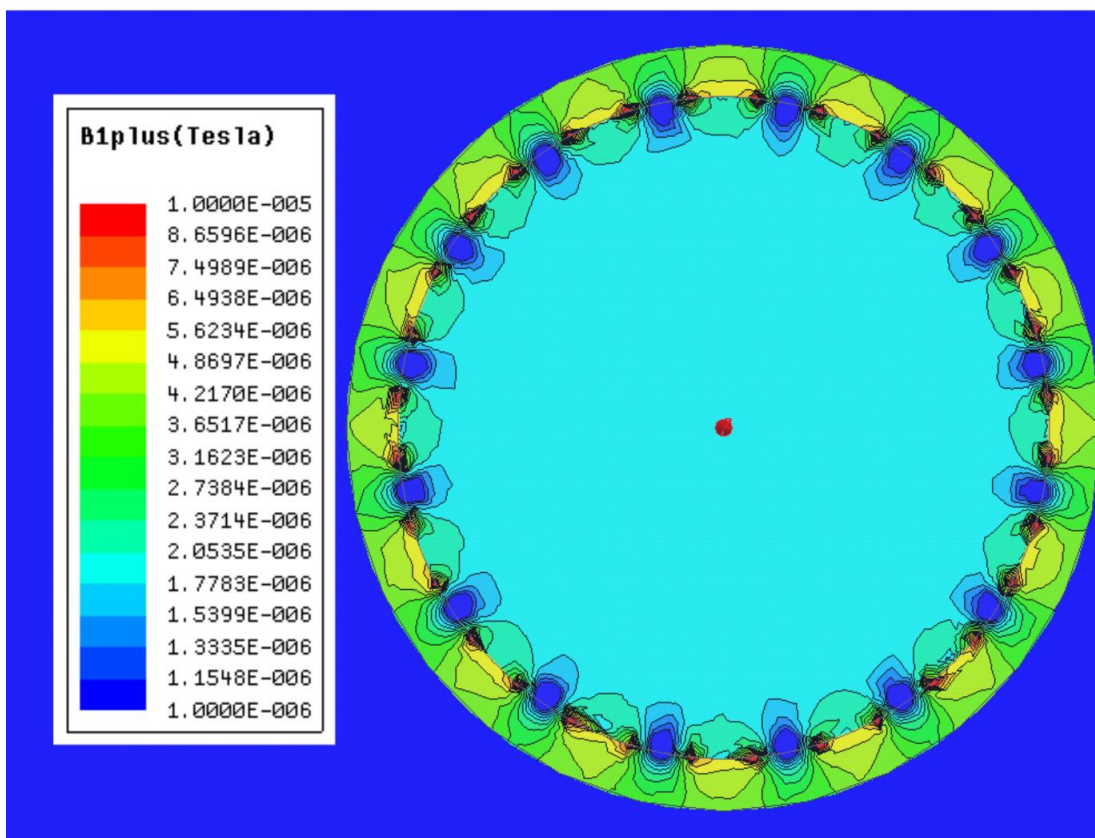
Figure 23: The simulated magnetic field in an unloaded coil

Table 3: Example of mesh refinement during simulation to produce solution convergence

Pass	Number of tetrahedra	Max Magnitude of delta S	Memory Used (GB)
1	40,641	N/A	2.85
2	52,835	0.48814	3.66
3	68,690	0.12984	4.91
4	89,301	0.0529	6.75
5	113,286	0.029266	8.67
6	147,272	0.010708	11.7
7	191,455	0.0041845	15.4
8	248,897	0.0022001	19.2

SAR

The ***local SAR*** (W/kg) is defined through averaging the dissipated power per unit mass over a small (ideally infinitesimally small) volume V, that is

$$SAR(\boldsymbol{r}) = \frac{1}{V}\int_{V}\frac{\sigma(\boldsymbol{r})}{2\rho(\boldsymbol{r})}|\boldsymbol{E}(\boldsymbol{r})|^2 dV \tag{1a}$$

Here, $\sigma(\boldsymbol{r})$ is the local tissue conductivity, $\rho(\boldsymbol{r})$ is the local mass density, and $|\boldsymbol{E}(\boldsymbol{r})|$ is the electric field magnitude at the observation point. The ***body-averaged or the whole-body*** SAR_{body} is given by averaging over the entire body volume, as

$$SAR_{body} = \frac{1}{V_{body}}\int_{V_{body}}\frac{\sigma(\boldsymbol{r})}{2\rho(\boldsymbol{r})}|\boldsymbol{E}(\boldsymbol{r})|^2 dV \tag{1b}$$

Similarly, SAR_{1g} is given by averaging over a volume with the weight of 1 g

$$SAR_{1g}(\boldsymbol{r}) = \frac{1}{V_{1g}} \int_{V_{1g}} \frac{\sigma(\boldsymbol{r})}{2\rho(\boldsymbol{r})} |\boldsymbol{E}(\boldsymbol{r})|^2 dV \qquad (1c)$$

$SAR_{10g}(\boldsymbol{r})$ is found in a similar fashion.

Human body properties for electromagnetic simulations and their dependence on frequency are the subject of active research and reasonably well documented [13]-[18].

An example simulation conducted using merely an empty skin shell (i.e., homogenous skin material throughout the skin volume) is given in Figure 24 below. This was constructed as a base simulation case to verify that the model was running well and as a means of comparing other non-homogeneous cases.
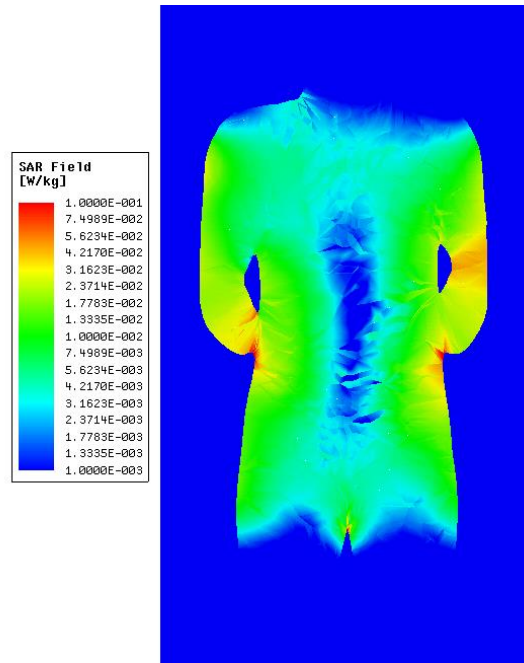
Figure 24: The local SAR experienced by a homogenous skin shell in an MRI coil

Future Work

The future applications of this project involve any number of simulations that call for the inclusion of the VHP Male CAD model that resulted from this project. Analysis and testing in the biomedical field is the most notable application for this model, specifically the effects of MRI scans on the body and on orthopedic implants. Another potential application for the model is simulating how the human body interacts with Bluetooth radio waves, which could lead to better designs for Bluetooth headphones.

Additionally, the entirety or parts of the process of this project can be redone in different ways to improve results for the same or different applications. This report and the resulting bone meshes from this project provide information and starting points that would assist such an endeavor.

To further develop the results of this project, more virtual tissues need to be included in the model. In other words, processed meshes representing more tissues or tissue types than the ones generated through this project and included in this project need to be created and/or added to the model for simulation. This is one way to more fully and more accurately understand how certain electromagnetic waves are affected by or affect the human body.

Conclusion

The goal for this Major Qualifying Project was to create a virtual CAD model that accurately represents the human male body so that medical computational electromagnetic simulations could be run on the model. This model was successfully created and simulated on. Creating this model involved processing 180 bone meshes that represent the entirety of the cortical bone in the human skeleton and combining those meshes with previously processed

meshes that represent other human tissue layers like cartilage, skin, and organs. Simulations were run on this model and the data shows promise for the model's usefulness.

References

Virtual Humans

[1]   M.J. Ackerman, "The Visible Human Project®: From Body to Bits," 38th Annual Int. Conf. of the IEEE Engineering in Medicine and Biology Society, Orlando, FL, Aug. 16-21, 2016.

[2]   "The Visible Human Project - Color Cryosections", *Nlm.nih.gov*, 2017. [Online]. Available: https://www.nlm.nih.gov/research/visible/photos.html. [Accessed: 04- Apr- 2017].

[3]   The Visible Human Project, U.S. National Library of Medicine. Available: https://www.nlm.nih.gov/research/visible/getting_data.html

[4]   National Institute of Biomedical Imaging and Bioengineering, NIH: "Computational Modeling," Sept. 2016. Available: https://www.nibib.nih.gov/science-education/science-topics/computational-modeling

[5]   U.S. Food and Drug Administration, Center for Devices and Radiological Health "Reporting of Computational Modeling Studies in Medical Device Submissions: Draft Guidance for Industry and Food and Drug Administration Staff," Sept. 2016. Available: http://www.fda.gov/downloads/MedicalDevices/DeviceRegulationandGuidance/GuidanceDocuments/UCM381813.pdf

[6]   J. Wismans, R. Happee and J. A. W. van Dommelen. "Computational human body models," in Anonymous 2005. DOI: 10.1007/1-4020-3796-1_43.

[7]   L. Science, "Digital AustinMan Created to Study Cell Phone Radiation," *Live Science*, 2017. [Online]. Available: http://www.livescience.com/19554-austin-man-radiation-nsf-bts.html. [Accessed: 04- Apr- 2017].

[8]   "IsoSurface | Scientific Volume Imaging," *Svi.nl*, 2017. [Online]. Available: https://svi.nl/IsoSurface. [Accessed: 04- Apr- 2017].

[9]   "Computational human phantom," *En.wikipedia.org*, 2017. [Online]. Available: https://en.wikipedia.org/wiki/Computational_human_phantom. [Accessed: 04- Apr- 2017].

[10]   S. Patil, "Voxel-based Solid Models: Representation, Display and Geometric

Analysis," 2017. [Online]. Available:
https://pdfs.semanticscholar.org/b2ec/9d0c9fadba4174e1ae5d29fccb7b344dc365.pdf.
[Accessed: 04- Apr- 2017].

[11]   T. Möller and B. Trumbore, "Fast, Minimum Storage Ray/Triangle
Intersection," J. of Graphics Tools, vol. 2, pp. 21–28, 1997.

[12]   C. Dennis, "What is Non-Manifold Geometry?", *TransMagic*, 2013. [Online].
Available: https://transmagic.com/what-is-non-manifold-geometry/. [Accessed: 04- Apr-
2017].

Electromagnetic Properties of Body Tissues

[13]   C. Gabriel, "Compilation of the dielectric properties of body tissues at RF and
microwave frequencies," Armstrong Laboratory, Brooks Air Force Base, Tech. Rep.
AL/OE-TR-1996-0037, 1996.

[14]   C. Gabriel, S. Gabriel, and E. Corthout, "The dielectric properties of biological
tissues: I. Literature survey," Phys. Med. Biol, vol. 41, pp. 2231-2249, Nov.1996.

[15]   S. Gabriel, R. W. Lau, and C. Gabriel, "The dielectric properties of biological
tissues: II. Measurements in the frequency range 10 Hz to 20 GHz," Phys. Med. Biol., vol.
41, pp. 2251-2269, Nov.1996.

[16]   S. Gabriel, R. W. Lau, and C. Gabriel, "The dielectric properties of biological
tissues: III. Parametric models for the dielectric spectrum of tissues," Phys. Med. Biol., vol.
41, pp. 2271-2293, Nov.1996.

[17]   C. Gabriel, A. Peyman, and E. H. Grant, "Electrical conductivity of tissue at
frequencies below 1 MHz," Phys. Med. Biol., vol. 54, pp. 4863-78, Aug. 2009.

[18]   Hasgall PA, Baumgartner C, Neufeld E, Gosselin MC, Payne D, Klingenböck A,
Kuster N. *IT'IS Database for thermal and electromagnetic parameters of biological
tissues*. Available from: https://www.itis.ethz.ch/database.

Transcranial Magnetic Stimulation

[19]   Wagner, T., A. Valero-Cabre, and A. Pascual-Leone, *Noninvasive human brain
stimulation.* Annu Rev Biomed Eng, 2007. **9**: p. 527-65.

[20]   Barker, A.T., R. Jalinous, and I.L. Freeston, *Non-invasive magnetic stimulation of
human motor cortex.* Lancet, 1985. **1**(8437): p. 1106-7.

RF Heating

[21]   U.D. Monu, P.W. Worters, B.A. Hargreaves, and G.E. Gold, "Radiofrequency
Induced Heating On or Near Passive Metallic Implants at 1.5T and 3.0T," *ORS 2012*

Annual Meeting.

[22]   H. Muranaka, T. Horiguchi, S. Usui, Y. Ueda, O. Nakamura, F. Ikeda, K. Iwakura, and G. Nakaya, "Evaluation of RF heating on humerus implant in phantoms during 1.5 T MRI imagining and comparisons with electromagnetic simulation," *Magn Reson Med Sci.*, vol. 5(2), pp. 79-88, July 2006.

[23]   H. Muranaka, T. Horiguchi, S. Usui, Y. Ueda, O. Nakamura, and F. Ikeda, "Dependence of RF heating on SAR and implant position in a 1.5T MR system," *Magn Reson Med Sci.*, vol. 6(4), pp. 199-209, 2007.

Use of Computational Phantoms in MRI

[24]   E. Lucano, M. Liberti, G. G. Mendoza, T. Lloyd, M. I. Iacono, F. Apollonio, S. Wedan, W. Kainz, and L. M. Angelone, "Assessing the Electromagnetic Fields Generated By a Radiofrequency MRI Body Coil at 64 MHz: Defeaturing Versus Accuracy," *IEEE Trans. Biomedical Eng.*, vol. 63, no. 8, pp. 1591-1601, 2016.

[25]   C. M. Patel, *SAR Map of Gel Phantom in a 64MHz MRI Birdcage by Fiber-Optic Thermometry and FDTD*, MS Thesis, California Polytechnic State University, CA, USA, 2011.

[26]   K. Thiyagarajan, T. Kesavamurthy, and G. Bharathkumar, "Design and Analysis of Microstrip-Based RF Birdcage Coil for 1.5 T Magnetic Resonance Imaging," *Appl Magn Resonance*, vol. 45, pp. 255–268, 2014.

[27]   N. Gurler and Y. Z. Ider, "FEM based Design and Simulation Tool for MRI Birdcage Coils including Eigenfrequency Analysis," *Proc. of the 2012 COMSOL Conf.*, Milan, Italy.

[28]   A. Obi, *Method of Moments Approach for the Design of RF Coils for MRI*, PhD Thesis, Worcester Polytechnic Inst., Worcester, MA 2008.

[29]   P. Serano, *Design of a Multi-Array Radio-Frequency Coil for Interventional MRI of the Female Breast*, MS Thesis, Worcester Polytechnic Inst., Worcester, MA 2009.

[30]   H. Muranaka, T. Horiguchi, Y.Ueda, and N. Tanki, "Evaluation of RF heating due to various implants during MR procedures," *Magn Reson Med Sci.*, vol. 10(1), pp. 11-19, 2011.

[31]   A. Kyriakou, A. Christ, E. Neufeld, and N. Kuster, "Local TissueTemperature Increase of a Generic Implant Compared to the Basic Restrictions Defined in Safety Guidelines," *Bioelectromagnetics*, vol. 33, pp. 366-374, 2012.

[32]   S. Akoka, F. Franconi, F. Seguin, and A. Le Pape, "Radiofrequency map of an NMR coil by imaging," Magn. Reson. Imag., vol. 11, no. 3, pp. 437–441, 1993.

[33]   G. Helms, J. Finsterbusch, N.Weiskopf, and P. Dechent, "Rapid radiofrequency field mapping in vivo using single-shot STEAM MRI," *Magn. Reson. Med.*, vol. 60, no. 3, pp. 739–743, 2008.

[34]   K. Nehrke and P. Bornert, "DREAM—A novel approach for robust, ultrafast,

multislice B1 mapping," *Magn. Reson. Med.*, vol. 68, no. 5, pp. 1517–1526, 2012.

[35]   T. Voigt, H. Homann, U. Katscher, and O. Doessel, "Patient-individual local SAR determination: In vivo measurements and numerical validation," *Magn. Reson. Med.*, vol. 68, no. 4, pp. 1117–1126, 2012.

[36]   X. Zhang, P.-F. V. de Moortele, S. Schmitter, and B. He, "Complex B1 mapping and electrical properties imaging of the human brain using a 16-channel transceiver coil at 7 T," Magn. Reson. Med., vol. 69, no. 5, pp. 1285–1296, 2013.

[37]   Homann H. SAR Prediction and SAR Management for Parallel Transmit MRI. Karlsruhe Translations on Biomedical Eng. 2012; 16: 1-124

[38]   H. Homann, P. Börnert, H.Eggers, K. Nehrke, O. Dössel, and I. Graesslin, "Towards Individualized SAR Models and in vivo Validation," Magn. Reson. Med., vol. 66, pp. 1767–1776, 2011.

[39]   G. Tiberi, M. Costagli, L. Biagi, A De Ciantis, N. Fontana, R. Stara, M. R. Symms, M. Cosottini, R. Guerrini, and M. Tosetti, "SAR Prediction in Adults and Children by Combining Measured B1+ Maps and Simulations at 7.0 Tesla," *J. Magnetic Res. Imaging*, vol. 44, no. 4, pp. 1048-1055, 2016.

[40]   R. Stollberger and P. Wach, "Imaging of the active B1 field in vivo," *Magn Reson Med.* vol. 35, no 2, pp. 246-51, Feb. 1996.

[41]   S. Oh, Y.-C. Ryu, G. Carluccio, C. T. Sica, and C. M. Collins, "Measurement of SAR-induced temperature increase in a phantom and in vivo with comparison to numerical simulation," *Magn. Reson. Med.*, vol. 71(5), pp. 1923–1931, May 2014.

[42]   A. T. Mobashsher, A. M. Abbosh, "Artificial Human Phantoms: Human proxy in testing microwave apparatus that have electromagnetic interaction with the human body," IEEE Microwave Magazine, vol. 16, no. 6, pp. 42-62, July 2015.

Other

[43]   M. Salzle, "PCL Developers Blog," Pointclouds.org, 2012. [Online]. Available: http://pointclouds.org/blog/nvcs/martin/index.php. [Accessed: 25- Apr- 2017].